The Influence of Laminar-Turbulent Transition on Rotor Performance at Low Reynolds Numbers

Finbar J. Argus[1]

farg967@aucklanduni.ac.nz, University of Auckland, Auckland, New Zealand

Geoffrey A. Ament[2]

NASA Ames Research Center, Moffett Field, California, U.S

Witold J. F. Koning[3]

Science and Technology Corporation, NASA Ames Research Center, Moffett Field, California, U.S

Laminar-turbulent transition can significantly affect rotor performance at low Reynolds numbers by altering the presence and extent of laminar boundary layer separation. This effect can cause the performance of small unmanned aerial vehicles and micro air vehicles to be significantly dependent on freestream turbulence intensity, rotor surface roughness, and rotor vibrations. To understand the extent of this effect, 2D airfoil decks with varying critical amplification factors were created using XFOIL and its e^N transition model. The decks were implemented into a 3D flow solver that couples a RANS flow solution with a Blade Element Theory model. This allowed rotor performance to be evaluated over sweeps of critical amplification factor and Reynolds number. At chord-based Reynolds numbers between $Re_{3/4} = 2 \times 10^4$ and $Re_{3/4} = 8 \times 10^4$, increasing the critical amplification factor from 3 to 11 is shown to decrease the figure of merit of the rotor in hover by approximately 40%. Forward flight simulations also show an equivalent drop in performance. However, the influence of critical amplification factor on roll moment in forward flight was found to be less than 10% of the roll moment generated by the forward velocity. Simulated airfoil boundary layer growth is displayed to detail the laminar separation that causes the extensive drop in performance at low Reynolds numbers. Good agreement is shown between simulation and experiment for earth atmospheric pressure. The results of this study show that conventional airfoil rotors are strongly influenced by the operating condition for Reynolds numbers below 1.2×10^5 and that future work needs to be done on design and testing of low Reynolds number rotor blades.

Nomenclature

C_D	=	airfoil drag coefficient
C_L	=	airfoil lift coefficient
C_M	=	airfoil moment coefficient
C_P	=	coefficient of pressure
Ma	=	Mach number
N	=	amplification factor in the e^N method
N_{Crit}	=	critical amplification factor
P	=	static pressure
r	=	rotor radial coordinate
R	=	rotor radius
R_g	=	gas constant
Re	=	Reynolds number
Re_c	=	chord-based Re

[1] PhD candidate. Auckland Bioengineering Institute
[2] Controls Engineer, Aeromechanics Branch, NASA Ames Research Center
[3] Aerospace Engineer, Aeromechanics Branch, NASA Ames Research Center

Presented at the VFS Aeromechanics for Advanced Vertical Flight Technical Meeting, San Jose, CA, January 21–23, 2020.

$Re_{3/4}$	=	chord-based Re at $r = 3/4R$, in hover
T	=	temperature
Tu_∞	=	free stream turbulence intensity %
V	=	forward flight velocity
x	=	normalized chord location
α	=	angle of attack
ρ_∞	=	freestream density
μ	=	dynamic viscosity

Introduction

Airfoils at a low Reynolds Number (Re) have a sensitivity to operating conditions such as freestream turbulence intensity (FST), rotor vibrations, rotor blade aeroelastic effects, and airfoil surface roughness. These parameters are accounted for by the N_{Crit} value, which is a measure of the disturbance amplification required to induce laminar-turbulent transition. This is further described in section "Boundary layer transition". For flow over airfoils with high N_{crit} and low Re, transition is delayed past the point of pressure recovery, and thus laminar separation can occur. This can cause an increase in drag and a decrease in lift. As of yet, little work has been done to analyze how this effect influences the performance of rotor blades. This study aims to show that rotor performance can be significantly affected by the operating condition at low Re.

Possibly the most important effect that needs to be understood occurs in the region between moderate to high Re, predominantly turbulent flow and low Re, predominantly laminar flow. In this region, the complex behavior of boundary layer separation, reattachment, and laminar separation bubbles (LSB) can have significant aerodynamic effects[1,2]. Specifically, the LSB can burst, resulting in full laminar separation, which can cause a substantial decrease in lift and increase in drag[3,4]. This bubble bursting could be the change from a short, steady LSB to a (time-averaged) unsteady LSB and could indicate the onset of vortex shedding[5]. Assuming the negative effects of laminar separation translate to rotor blades, there could be extreme drops in rotor performance at low Re.

Rotors that operate in a low chord-based Reynolds number regime ($Re_C < 10^5$) include small wind turbines, small unmanned aerial vehicles (UAV), and micro air vehicles (MAV). Extensive commercial and research developments in these areas make it essential to improve understanding of low Re_C rotor flight. Improved understanding will aid in optimizing low Re airfoils and designing safe control algorithms to avoid undesirable flight conditions. Another need for increased understanding is for low-pressure extra-terrestrial flight, such as that of the Mars Helicopter.[6,7]

The rotor used in this study has a radius of 0.508m, which was chosen to be similar to that of the Mars Helicopter (MH) developed by the Jet Propulsion Laboratory. Koning, Johnson, and Allan showed that the MH airfoil is unlikely to have a laminar-turbulent transition in Mars atmospheric conditions and that the flow is expected to remain predominantly laminar over the rotor in hover.[7] Therefore, in the current study a numerical analyses is conducted which focuses on higher Re ($2 \times 10^4 < Re < 2 \times 10^5$) hover for Earth-based applications.

Studies on low $Re_{3/4}$ for forward flight are scarce. A numerical study of forward flight is presented to show the drop in performance that occurs due to the retreating blade dropping into the critical Re region.

During forward flight, large roll moments can occur due to the imbalance in thrust between retreating and advancing blades. As forward speed increases, the retreating blade thrust decreases and the advancing blade thrust increases, causing a large roll moment. Helicopter rotors have cyclic control for this reason. However, many MAVs and UAVs do not have cyclic control and will therefore be very susceptible to this roll imbalance. Laminar separation on the retreating blade could strengthen this effect, resulting in larger roll moments. The extent of this effect is analyzed in this study.

Reynolds Number Effect on Aerodynamics

At high Re, airfoils typically have high lift and low drag due to the boundary layer experiencing laminar-turbulent transition close to the leading edge, delaying boundary layer separation. The turbulent boundary layer is chaotic and has small-scale eddying motion that causes transport of momentum from the freestream into the boundary layer. This turbulent exchange of momentum causes an increase in wall shear stress and time-averaged velocity.[8] A boundary layer with higher velocity and momentum can overcome a larger adverse pressure gradient and is thus less prone to separation. This reduction in separation causes increased thrust and decreased drag. Even though a turbulent boundary layer has a higher friction drag due to higher wall shear stress, it has a lower pressure drag due to the reduced separation. The decrease in pressure drag typically outweighs the increase in friction drag, resulting in lower total drag.[1] When Re drops below a critical Re laminar separation no longer occurs before the point of pressure recovery, which can result in laminar separation (the term 'critical' here is used as the termination of laminar separation).[9,10]

Low Reynolds Number Rotor Blades

Although substantial research has been conducted on low Re airfoils[11–16], few groups have extended this to rotors. Singh[17] took into account laminar separation and LSB when designing a low Re wind turbine. Bohorquez et al.[18] and Young et al.[19] analyzed MAV rotor performance at $Re_{3/4}$ below 5×10^4. Further work by Young et al.[6,20] presented the possibilities and limitations of rotorcraft that operate in the low-pressure Mars atmosphere. Escobar et al.[21] conducted analyses on Mars rotorcraft using a combination of vacuum chamber tests and free-wake based comprehensive analysis. None of these works, however, accounted for the performance sensitivity to operating condition or N_{Crit}. Koning and

Ament[22] analyzed forward flight simulations at low pressures and hence low $Re_{3/4}$. They found significant differences between prediction and experiment for thrust and power, which is likely due to their simulations not having a transition model and not accounting for the operating condition or N_{Crit}. Perez Perez[23] followed on from the work by Koning and Ament and showed improved comparisons with low-pressure experiments by using a fully laminar boundary layer assumption. Although this method may work at very low Re, a simulation method is needed that can account for operating condition dependent transition within the boundary layer.

Boundary layer transition

The onset of turbulence can be caused by a variety of effects as described by various theories.[1,24] Due to the relatively undisturbed flow being studied, a natural transition mechanism is assumed. In natural transition, the external disturbances in the free stream and the initial disturbances or oscillations in the boundary layer are assumed to be weak. Flow instabilities amplify the initial disturbances and cause them to increase exponentially in amplitude downstream and eventually become chaotic. The start of chaotic flow defines the laminar-turbulent transition. To predict the transition location for natural transition an e^N method can be used.

XFOIL, a software developed by Drela[25], is used in this study to calculate the drag and lift coefficients of many airfoil section configurations. This software uses the e^N method to predict the transition location caused by linear instability growth. The most common type of instability growth are Tollmien-Schlichting (TS) waves, which are sinusoidally-oscillating pressure and velocity perturbations within the boundary layer.[8] TS waves initially have small amplitudes near the leading edge, however, in unstable conditions they can grow exponentially. The amplification of the waves is defined by e^N, where N is the so-called "N-factor" in the e^N method.

XFOIL assumes that TS waves are the dominant type of instability growth. In the approximate envelope method, used in XFOIL, the e^N method is simplified by tracking only the maximum amplitudes of the most amplified frequencies.[16,26] The approximate envelope method simplifies the stability theory, transition model to only require tracking of one parameter, N, in the boundary layer. Once e^N reaches $e^{N_{Crit}}$, transition occurs. Therefore, N_{Crit} can be thought of as a quantification of the disturbance amplification required to cause transition. Equally, N_{Crit} can account for a combination of the receptivity and the size of the initial disturbances. Increased receptivity, which is influenced by surface roughness and vibrations, causes lower N_{Crit} due to increased influence of external disturbances on the boundary layer. Boundary layer flow with large initial disturbances, or equivalently high FST, requires less amplification to reach an amplitude that initiates transition, thus also has a lower N_{Crit}.

If the assumption that FST is the main operating condition effect, an N_{Crit} value can be found that is related to the percent of freestream turbulence intensity (Tu_∞). Drela[27] formulated a relation for this, which is presented in Eqs.1-2.

$$\tau = 2.7\tanh\quad (Tu\infty/2.7) \tag{1}$$

$$N_{Crit}(\tau) = -8.43 - 2.4\ln\left(\frac{\tau}{100}\right) \tag{2}$$

An N_{Crit} value of 11 translates to a Tu_∞ value of 0.03%, which is typical for very clean flow, such as a sailplane in flight. An N_{Crit} value of 9 translates to a Tu_∞ value of 0.07%, which is appropriate for the flow in a very quiet wind tunnel. Finally, an N_{Crit} value of 5 relates to a Tu_∞ value of 0.37%, which corresponds to a reasonably turbulent environment, such as in a noisy wind tunnel. Setting the N_{Crit} value to 1 can also be done to simulate bypass transition. This causes transition to occur immediately after linear instability begins.

XFOIL is effective at modelling airfoils in the range of this study, greater than $Re = 20000$. However, XFOIL is not as accurate for ultra-low Re. Drela[28] shows that XFOIL's first-order stability theory approach diverges from experimental results for Re below approximately 10000. In the same work, Drela details a second-order approach that resolves the issue. If a similar approach as this study was to be done for ultra-low Re, a higher-order implementation should be used.

Computational Approach

To analyze rotor performance a computational pipeline was set up. A schematic of this pipeline is shown in Fig. 1. This section details the operating parameters for the cases in the study, as well as a description of each step in the simulation pipeline.

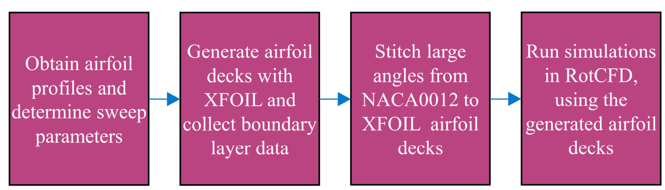

Fig. 1 Flow-chart of the simulation pipeline

Case studies

Three cases are run in this study, earth atmosphere hover (EAH), low-pressure sweep hover (PSH) and low-pressure sweep forward flight (PSFF). Table 1 shows the relevant parameters for each case.

Table 1 Case study parameters

	EAH	PSH	PSFF
$P\ [kPa]$	101.3	$4-40$	$4-40$
$\rho_\infty\ [kg/m^3]$	1.225	$0.0481-0.481$	$0.0481-0.481$
$T\ [K]$	290	290	290
$R_g [m^2/s^2/K]$	287	287	287
$\mu\ [Ns/m^2]$	1.75×10^{-5}	1.75×10^{-5}	1.75×10^{-5}
RPM	$250-4000$	3000	3000
$V[m/s]$	0	0	30

Blade Sections

For this study the airfoil profiles were obtained using the CreaformMetraScan-70, a 3D optical laser scanner. Profile curves were then fit to the resulting point cloud to obtain 2D airfoil sections. Works by Koning[29], and Perez Perez[30] detail the selection of critical airfoil sections and the geometric parameters of the blade. In this study, as in Perez' work, the critical airfoil sections were chosen as $r/R = 0.29, 0.58, 0.78$ and 0.95.

Airfoil Deck Generation, XFOIL

An airfoil deck stores the lift, drag, and moment coefficients for 2D airfoil profiles at a range of Ma and α. To create these decks, a Python application was developed to automate the running of XFOIL and sweep through α, Ma, airfoil section, N_{Crit}, and pressure. The application outputs airfoil decks as well as boundary layer parameters. These parameters allow analysis and visualization of the transition and separation behavior. This study required more than 400 airfoil decks, each deck requiring 217 2D flow simulations. This would have been infeasible for a Reynolds Averaged Navier-Stokes (RANS) 2D solver to generate. Therefore, the speed of the Python-XFOIL application allowed for a more refined study than could have been done with typical airfoil deck generation software.

Each airfoil deck generation requires solving for the lift and drag coefficients for α from -10 to 20 in steps of 1 and Ma of 0.05 and 0.1 to 0.6 in steps of 0.1. Generating one airfoil deck with this Python-XFOIL application takes approximately 30 minutes on a 3.60 GHz processor node of a standard desktop workstation. In comparison, on the same workstation, the airfoil deck generation software C81gen takes on the order of days to generate one airfoil deck, depending on the airfoil. Therefore, compared to C81gen, the Python-XFOIL application developed in this study shows a factor of over 100x improvement in runtime. In future work the application will be updated to allow parallel processing, further improving the computational speed.

RANS Grid Resolution Study

To analyze the full 3D rotor behavior, the airfoil decks are used with a mid-fidelity RANS solver RotCFD.[31] This solver uses an unsteady RANS model coupled with a Blade Element Momentum theory model. The software solves for the velocity and pressure throughout the computational domain and the time averaged forces and moments on the blades.

To ensure the grids used in this study were sufficiently refined, grid resolution studies were done for both hover and forward flight. The number of cells was increased until the thrust, power and hover Figure of Merit (FM) changed by less than 1%. The resulting grids for hover and forward flight are shown in Fig. 2. For both cases, all boundaries were set as fixed velocity conditions apart from the outflow boundary, which was set as a mass outflow correction boundary condition. In hover the outflow wall was the bottom boundary, whereas in forward flight it was the downstream wall. For forward flight the rotor was pitched forward by 14 degrees to simulate realistic flight.

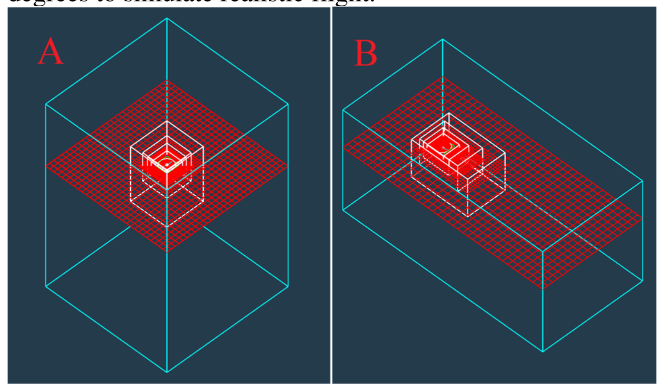

Fig. 2 RotCFD grid for (A) hover and (B) forward flight

Experimental Approach

Hover test data presented in this paper were conducted in the Planetary Aeolian Laboratory (PAL) at NASA Ames, where pressures as low as $550 Pa$ can be reached by evacuating air from the facility. For this study, thrust, torque, and power data at earth atmospheric pressure ($101.3\ kPa$) are presented. Future tests are to be done at a range of pressures from $1\ kPa$ to $40\ kPa$. Details on the rotor, the facility, the hardware, and the sensors used in this study can be found in Ament and Koning's work.[22] Their study made use of the Martian Surface Wind Tunnel, located in the PAL to analyze a rotor in forward flight, whereas in the current study the same rotor was moved out of the wind tunnel to attempt to analyze hover without wall effects. In the current work, the rotor, as shown in Fig. 3, was set up in a thrusting up orientation, 3.2m off the ground, more than 3.5m from the closest wall, and more than 15m from the ceiling.

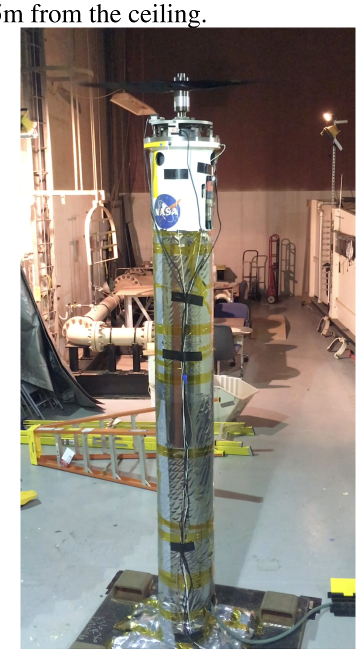

Fig. 3 Hover experimental setup in the Planetary Aeolian Laboratory.

Hover Experimental Results

Tests were conducted for the EAH case, with one (2-bladed rotor) and two (4-bladed co-rotating rotor) propellers. The resulting plots for thrust vs RPM^2, torque vs RPM^2, and power vs RPM^3 are presented in Figs. 4-6. The two-propeller tests were limited to 3000 RPM to keep the load cells below their rated limit.

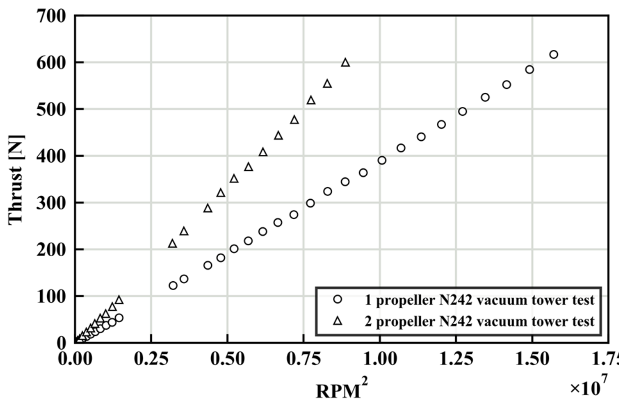

Fig. 4 Experimental thrust vs RPM^2 for Earth atmosphere hover.

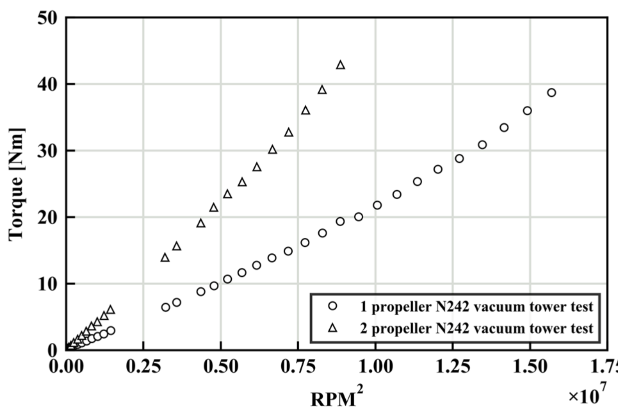

Fig. 5 Experimental torque vs RPM^2 for Earth atmosphere hover.

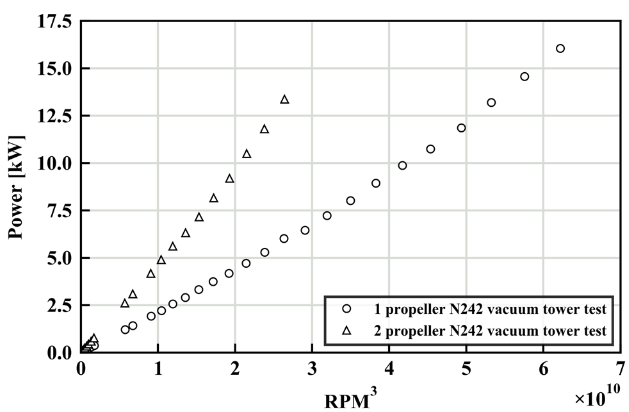

Fig. 6 Experimental power vs RPM^2 for Earth atmosphere hover.

Hover Simulation Results

Hover simulations were performed at both Earth atmosphere (EAH) for validation and low pressures (PSH) to analyze low $Re_{3/4}$ performance. Due to computational cost, the simulations were only done for 1 propeller stack (2-bladed rotor). Also, to ensure a tip Ma below 0.65, a constant RPM of 3000 RPM was chosen.

Validation at Earth atmosphere (EAH)

Comparisons at $101.3\,kPa$ were done to ensure the simulations were accurate in standard flight conditions. Figs. 7-9 show the thrust vs RPM^2, power vs RPM^2 and power vs thrust plots, respectively. The simulations were evaluated for N_{Crit} values of 2, 5, 9 and 11. The results with N_{Crit} values of 9 and 11 matched well with experiment, having median thrust errors of 4% and 2%, respectively. An N_{Crit} value of 9 corresponds with a clean wind tunnel and an N_{Crit} value of 11 translates to very smooth operating conditions, such as flying through still air. Therefore, since the vacuum tower is large and has minimal flow recirculation, the N_{Crit} value of 11 giving the best results was not surprising. Also, centrifugal effects of rotor blades can have stabilizing effects and delay transition.[32] This could mean that rotor blades have relatively large N_{Crit} compared to fixed wings. However, the opposite could be argued for added vibrations and aeroelastic effects causing lower N_{Crit}. Future work should be done on correlating N_{Crit} with rotor flight conditions. The power vs thrust curve in Fig. 9 shows very good comparison for all N_{Crit}. The reason that the difference in simulation results between different N_{Crit} is relatively small is due to the large $Re_{3/4}$ of 5×10^5, which results in all cases transitioning before significant laminar separation can occur.

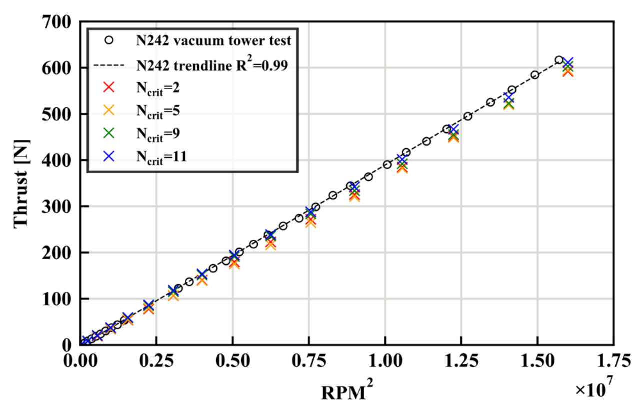

Fig. 7 Thrust vs RPM^2 at 101.3 kPa, comparison of simulations with experiments, Earth atmosphere hover.

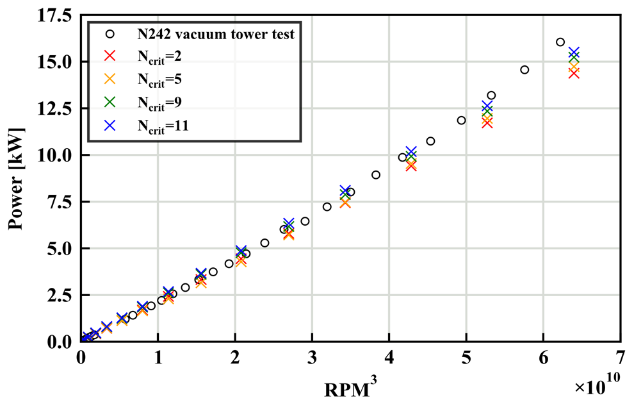

Fig. 8 Power vs RPM³ at 101.3 kPa, comparison of simulations with experiments, Earth atmosphere hover.

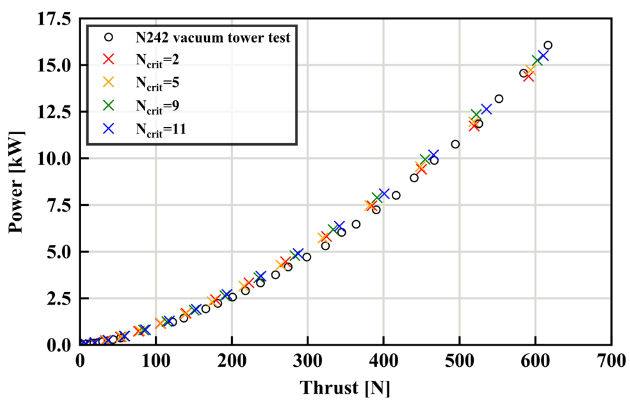

Fig. 9 Power vs thrust at 101.3 kPa, comparison of simulations with experiment, Earth atmosphere hover.

Interestingly, the power vs thrust trend in Fig. 9 is relatively unaffected by N_{Crit} at this high $Re_{3/4}$ due to higher N_{Crit} resulting in both increased thrust and increased power. The increased thrust is due to high N_{Crit} delaying transition and the increased power is due to an increase in induced drag due to the increased thrust. For supercritical Re, transition occurs before the point of pressure recovery, therefore, laminar separation is not a risk. The delay of transition caused by high N_{Crit} results in the turbulent boundary layer having less time to grow, resulting in delayed turbulent separation. The delayed separation causes lower pressures on the top surface and thus increased lift and hence thrust. During hover, induced drag dominates profile drag,[33] therefore, the increase in lift and hence increase in induced drag explains the increase in power for high N_{Crit}. The $Re_{3/4}$ at earth atmosphere does not drop low enough for significant laminar separation to occur, therefore N_{Crit} does not significantly affect performance. To see an influence of N_{Crit} on performance, lower $Re_{3/4}$ are analyzed.

Low Reynolds Number Rotor Performance (PSH)

A sweep over pressure, or equivalently $Re_{3/4}$, was simulated with six N_{Crit} values to determine its influence on rotor performance. Firstly, the thrust and power plots are presented against $Re_{3/4}$ in Figs. 10 and 11 respectively.

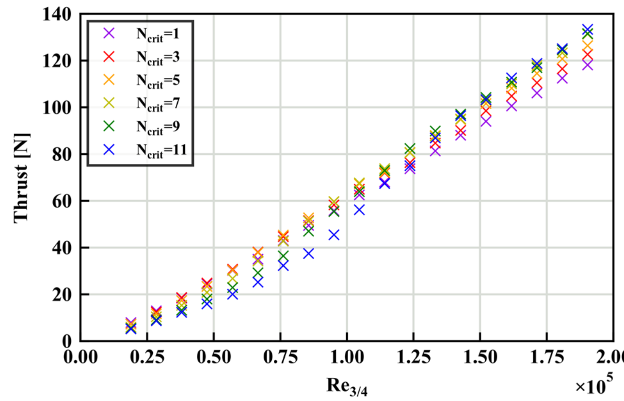

Fig. 10 Thrust vs ¾ radius Reynolds number at 3000 RPM, pressure sweep hover.

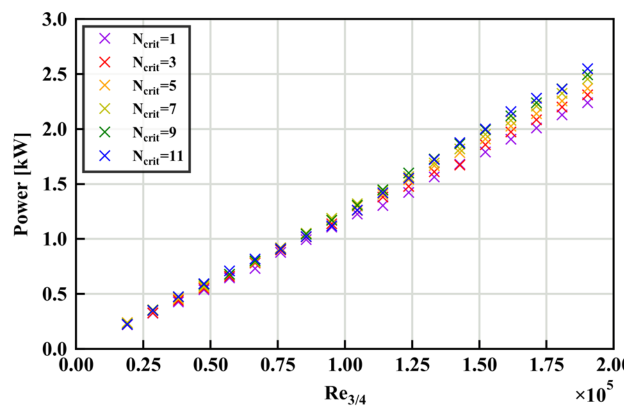

Fig. 11 Power vs ¾ radius Reynolds number at 3000 RPM, pressure sweep hover.

Similar to in earth atmosphere, the thrust and power at $Re_{3/4}$ greater than 1.2×10^5 is larger for higher N_{Crit}. The power, as seen in Fig. 11, does not show an inflection point at 1.2×10^5, however, the predictions in power seem to collapse and are independent of N_{Crit} below 1.2×10^5. The reason for this collapse is due to a balance between higher N_{Crit} increasing power due to increased drag from separation and higher N_{Crit} decreasing power due to decreased induced drag from the lower lift and thrust.

Fig. 10 shows a large drop in thrust for high N_{Crit} when $Re_{3/4}$ drops below approximately 1.2×10^5. The drop in performance related to this decrease in thrust below $Re_{3/4}$ of 1.2×10^5 is clearly seen in Fig. 12. A distinct drop in FM occurs for all N_{Crit} values as $Re_{3/4}$ is decreased, with higher N_{Crit} values reaching a critical laminar/turbulent transition region earlier. For $Re_{3/4}$ between 2×10^4 and 8×10^4 the FM drop between N_{Crit} values of 3 and 11 is approximately 40%. This shows the massive drop in performance that can occur at low Re between different operating conditions.

Multiple studies have shown the critical Re_C to be approximately 7×10^4.[3,4] This relates well with the critical $Re_{3/4}$ of approximately 1.2×10^5 found here, as when $Re_{3/4}$ drops below this value, significant parts of the blade experience a Re_C below 7×10^4. As $Re_{3/4}$ decreases further, more of the blade becomes subcritical, further decreasing performance.

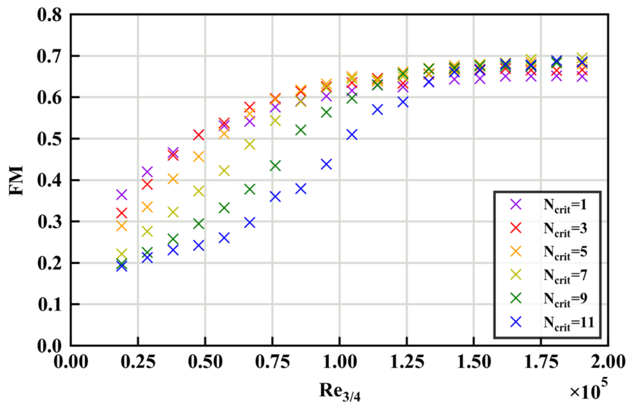

Fig. 12 Figure of merit vs 3/4 radius Reynolds number at 3000 RPM, pressure sweep hover.

Laminar Separation

The large drop in FM for high N_{Crit} at constant $Re_{3/4}$ is due to laminar separation. Laminar separation occurs for high N_{Crit} due to the shear layer remaining laminar past the point of pressure recovery. A laminar shear layer does not entrain momentum from the freestream, which results in shear layer separation from the blade quickly after it encounters an adverse pressure gradient. This effect can be seen clearly by comparing Figs. 13 and 14 for $N_{Crit} = 1$ and 11 respectively. Both results are for section $r/R = 0.78$, $Re_C = 6 \times 10^4$, $Ma = 0.5$ and $AoA = 7°$. The $N_{Crit} = 1$ case shows early transition before significant boundary layer growth can occur. The turbulent boundary layer after transition entrains the momentum from the freestream which reduces boundary layer growth. The $N_{Crit} = 11$ case shows massive shape factor and displacement thickness growth before transition, which is a clear sign of separation. Following separation, the separated shear layer transitions close to the trailing edge without reattachment. Reattachment does not occur after transition, as can be seen by the displacement thickness increasing. The absence of reattachment is due to the large size of the boundary layer.

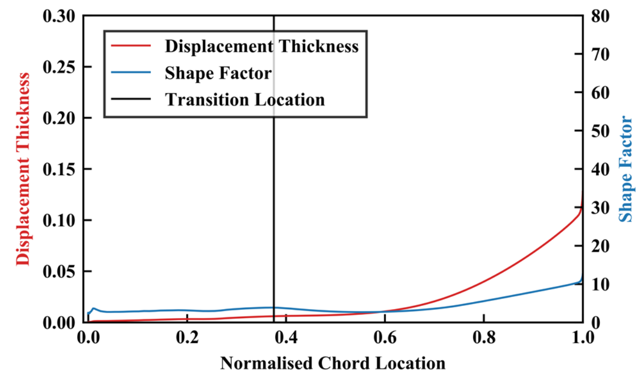

Fig. 13 Displacement thickness and shape factor vs the normalized chord location for $N_{Crit} = 1$.

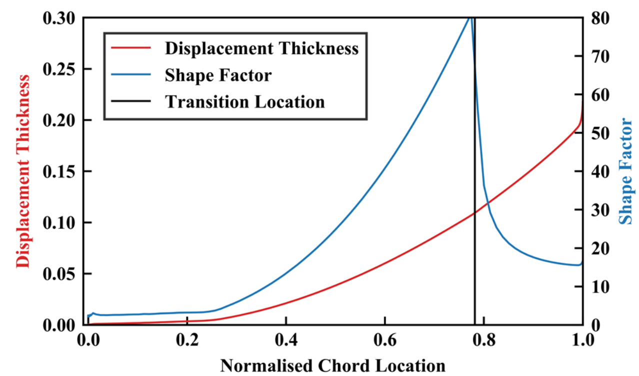

Fig. 14 Displacement thickness and shape factor vs the normalized chord location for $N_{Crit} = 11$.

For the same cases as Figs. 13-14, the coefficient of pressure and boundary layer velocity profiles are plotted in Figs. 15-16 for $N_{Crit} = 1$ and 11 respectively. For $N_{Crit} = 11$ the boundary layer velocity profiles show the flow staying attached and laminar until $x \approx 0.4$, then separating, as shown by the negative velocity at the wall. Compared to $N_{Crit} = 1$, this laminar separation causes C_P to become less negative on the top surface of the airfoil, which explains the drop in lift.

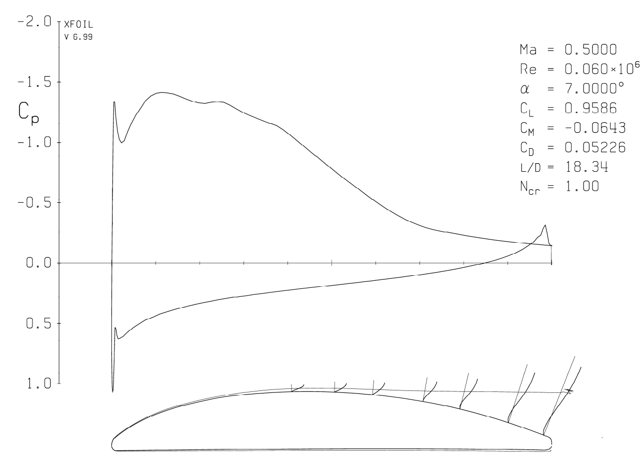

Fig. 15 Coefficient of pressure vs normalized chord location (top) and velocity profiles (bottom) for $N_{Crit} = 1$.

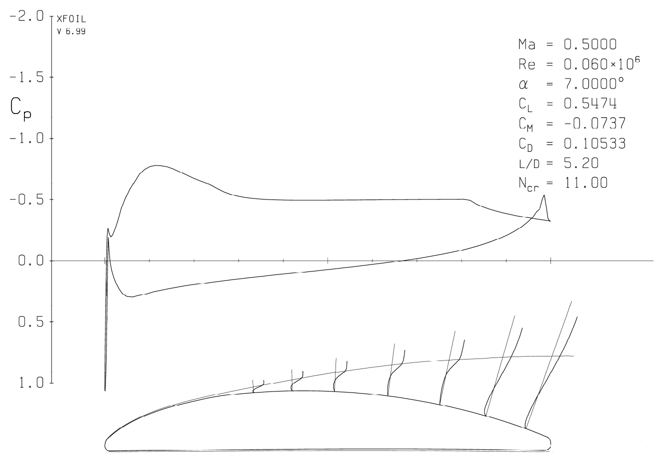

Fig. 16 Coefficient of pressure vs normalized chord location (top) and velocity profiles (bottom) for $N_{Crit} = 11$.

Numerical Forward Flight Results

Forward Flight Rotor Performance (PSFF)

The same sweep in pressure as in Figs. 10-12 was also done for the forward flight case. The thrust and power are plotted against the blades $Re_{3/4}$ in Figs. 17 and 18 respectively, where $Re_{3/4}$ does not account for the relative blade speeds in forward flight. Forward flight causes the retreating blade to have a lower relative velocity, therefore, a lower Re_C along the blade. This results in the retreating blade experiencing critical Re_C over large sections of the blade at a higher $Re_{3/4}$ than in hover. Therefore, the thrust drops at higher $Re_{3/4}$ for forward flight than for hover. The drop in thrust can be seen to start at $Re_{3/4}$ of approximately 1.4×10^5. The power again collapses to be similar for all N_{Crit} at $Re_{3/4}$ below 1.2×10^5. The decrease in thrust for high N_{Crit} at constant $Re_{3/4}$ thus leads to a drop in forward flight performance, like that of hover but over a wider $Re_{3/4}$ range.

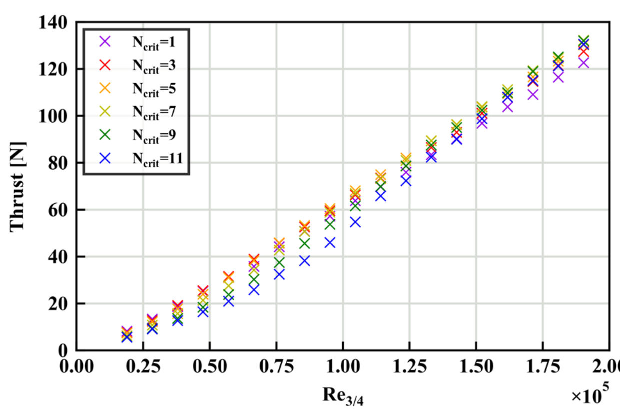

Fig. 17 Thrust vs ¾ radius Reynolds number at 3000 RPM for a 30m/s forward flight speed.

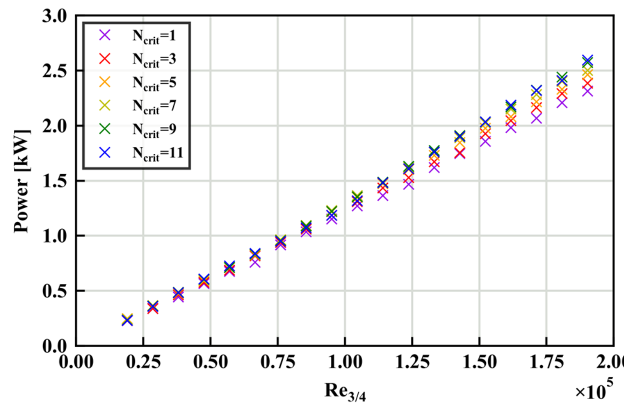

Fig. 18 Power vs ¾ radius Reynolds number at 3000 RPM for a 30m/s forward flight speed.

Forward Flight Roll Moment

The roll moment in forward flight is caused by a misbalance in thrust between the advancing blade and the retreating blade. Theoretically, this effect could be exaggerated depending on the operating condition. At high N_{Crit} the advancing blade could be predominantly supercritical, causing higher thrust and the retreating blade could be mostly subcritical, causing lower thrust. To test this hypothesis, the forward flight speed was varied for a constant RPM of 3000 and a constant pressure of 30 kPa. This pressure relates to a $Re_{3/4}$ of 1.4×10^5. The resulting roll moment vs forward flight speed plot is shown in Fig. 19. As expected, the cases with higher critical amplification have higher roll moments, which is due to two effects. Firstly, the advancing blade is predominantly supercritical, therefore, it produces higher thrust for a larger N_{Crit} due to delayed transition, as discussed in section "Validation at Earth atmosphere (EAH)". Secondly, the retreating blade is mostly subcritical, hence, it produces lower thrust for greater N_{Crit} due to laminar separation, as discussed in section "Laminar Separation". The combination of higher thrust on the advancing blade and lower thrust on the retreating blade results in larger roll moments for higher N_{Crit}. The difference in roll moment for $N_{Crit} = 3$ compared to $N_{Crit} = 11$ is approximately 10% of the moment created by the forward flight speed. Therefore, although the operating condition does have an influence on roll moment, it is minor compared to the roll moment created by forward flight speed.

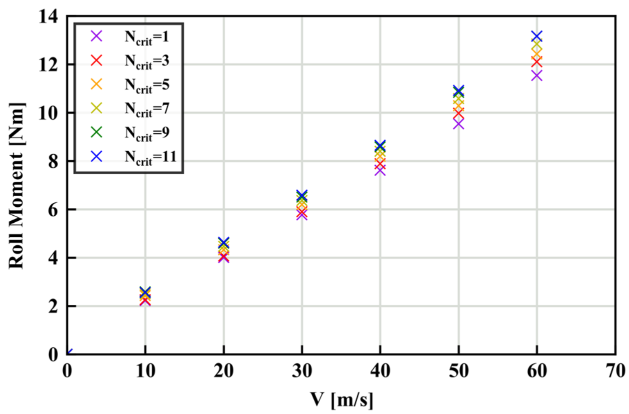

Fig. 19 Roll moment vs forward flight speed for 3000 RPM at 30 kPa.

Concluding Remarks

This paper shows that low $Re_{3/4}$ rotor blade performance is significantly affected by N_{Crit} and specifically by operating condition parameters such as FST, rotor vibrations, rotor blade aeroelastic effects, and airfoil surface roughness. The FM of rotors in hover conditions at $Re_{3/4}$ between 2×10^4 and 8×10^4 is shown to drop by approximately 40% between N_{Crit} values of 3 and 11. These results are relevant for MAV and small UAVs as well as future extraterrestrial flight. Forward flight is shown to have a similar drop in performance for a wider $Re_{3/4}$ range due to the retreating blade experiencing lower Re_C. Operating condition was also found to have a small effect on the roll moment during forward flight. Laminar separation is confirmed to be the cause for the drop in performance for high N_{Crit} at subcritical $Re_{3/4}$. Lower N_{Crit} and higher $Re_{3/4}$ cause transition to occur earlier, which aids in keeping the shear layer attached over the adverse pressure gradient region.

Acknowledgments

Firstly, I would like to thank Bill Warmbrodt for his support and enthusiasm, and the NASA Ames Aeromechanics branch for being a brilliant place to conduct research. My thanks also go to my supervisors at the Auckland Bioengineering Institute Peter Hunter, Christopher Bradley and Soroush Safaei. Also, my thanks go to The NASA International Internship Program and The NZ Space Agency for giving me the opportunity to collaborate with such brilliant people.

References

1. Drela, M. Flight Vehicle Aerodynamics. MIT Press, 2014.
2. Wang, S., Zhou, Y., Alam, M. M. & Yang, H. Turbulent intensity and Reynolds number effects on an airfoil at low Reynolds numbers. Physics of Fluids, 26, 2014.
3. Mueller, T. J. & DeLaurier, J. D. Aerodynamics of small vehicles. Annual review of fluid mechanics, 35, 2003.
4. Heathcote, S. & Gursul, I. Flexible flapping airfoil propulsion at low reynolds numbers. AIAA Journal, 45, 2007.
5. Pauley, L. L., Moin, P. & Reynolds, W. C. The structure of two-dimensional separation. Journal of fluid Mechanics, 220, 1990.
6. Young, L. A., Aiken, E., Lee, P. & Briggs, G. Mars rotorcraft: possibilities, limitations, and implications for human/robotic exploration. in IEEE Aerospace Conference, 2005.
7. Koning, W. J. F., Johnson, W. & Grip, H. F. Improved mars helicopter aerodynamic rotor model for comprehensive analyses. AIAA Journal, 57, 2019.
8. Schlichting, H. & Gersten, K. Boundary-layer theory. 2016.
9. Schmitz, F. W. Aerodynamics of the model airplane. 1967.
10. Hoerner, Sighard, F. Fluid Dynamic Lift - Practical Information on Aerodynamic and Hydrodynamic Lift. NASA STI/Recon Technical Report A, 1985.
11. Pelletier, A. & Mueller, T. J. Low Reynolds number aerodynamics of low aspect-ratio wings. 17th Applied Aerodynamics Conference, 37, 1999.
12. Alam, M. M., Zhou, Y., Yang, H. X., Guo, H. & Mi, J. The ultra-low Reynolds number airfoil wake. Experiments in Fluids, 48, 2010.
13. Mueller, T. J. & Batill, S. M. Experimental studies of the laminar separation bubble on a two-dimensional airfoil at low Reynolds numbers. AIAA Paper, 20, 1980.
14. Koning, W. J. F., Romander, E. A. & Johnson, W. Low reynolds number airfoil evaluation for the mars helicopter rotor. in Annual Forum Proceedings - AHS International, 2018.
15. Lissaman, P. B. S. Low-Reynolds-number airfoils. Annual Review of Fluid Mechanics, 15, 1983.
16. Drela, M. & Giles, M. B. Viscous-inviscid analysis of transonic and low Reynolds number airfoils. AIAA Journal, 25, 1987.
17. Singh, R. K. & Ahmed, M. R. Blade design and performance testing of a small wind turbine rotor for low wind speed applications. Renewable Energy, 50, 2013.
18. Bohorquez, F., Rankins, F., Baeder, J. D. & Pines, D. J. Hover performance of rotor blades at low reynolds numbers for rotary wing micro air vehicles. An experimental and CFD study. in 21st AIAA Applied Aerodynamics Conference, 2003.
19. Young, L. A. *et al.* New concepts and perspectives on micro-rotorcraft and small autonomous rotary-wing vehicles. in 20th AIAA Applied Aerodynamics Conference, June 2002.
20. Young, L. A., Aiken, E. W., Derby, M. R.,

Demblewski, R. & Navarrete, J. Experimental investigation and demonstration of rotary-wing technologies for flight in the atmosphere of Mars. in 58th Annual Forum of the AHS, International, Montreal, Canada, June 11-13, 2002.

21. Escobar, D. *et al.* Aeromechanical Loads on a Mars Coaxial Rotor.
22. Ament, G. A. & Koning, W. J. F. Isolated rotor forward flight testing from one atmosphere down to martian atmospheric densities. in Proceedings of the AHS International Technical Meeting on Aeromechanics Design for Transformative Vertical Flight, 2018.
23. Perez Perez, B. N. Forward flight rotor performance at martian atmospheric densities and sensitivity to low Reynolds numbers. in AHS Aeromechanics for Advanced Vertical Flight Technical Mtg, 2020.
24. Reed, H. L. Linear Stability Theory Applied to Boundary Layers. Annual Review of Fluid Mechanics, 28, 1996.
25. Drela, M. XFOIL: an analysis and design system for low Reynolds number airfoils. Low Reynolds Number Aerodynamics. Proc. Conf., Notre Dame, 1989.
26. Gleyzes, C., Cousteix, J. & Bonnet, J. L. Calculation method of leading-edge separation bubbles. in Numerical and Physical Aspects of Aerodynamic Flows II, 1984.
27. Drela, M. MISES implementation of modified Abu-Ghannam/Shaw transition criterion. MISES Code Documentation, MIT, 1998.
28. Drela, M. Higher-order boundary layer formulation and application to low Reynolds number flows. Fixed and Flapping Wing Aerodynamics for Micro Air Vehicle Applications, 195, 2001.
29. Koning, W. J. F. Generation of Performance Model for the Aeolian Wind Tunnel (AWT) Rotor at Reduced Pressure. NASA, 2018.
30. Perez Perez, B. N. Rotor CFD Analysis at Terrestrial and Martian Atmospheric Densities. 2018.
31. Rajagopalan, R. G. *et al.* RotCFD - A tool for aerodynamic interference of rotors: Validation and capabilities. in American Helicopter Society International - Future Vertical Lift Aircraft Design Conference, 2012.
32. Corrigan, J. J. & Schillings, J. J. Empirical Model for Stall Delay Due to Rotation. American Helicopter Society Aeromechanics Specialists Conference, 1994.
33. Johnson, W. Helicopter Theory. 2012.